

One-dimensional bichromatic standing-wave cooling of cesium atoms

A Camposeo¹, M Anderlini¹, D Ciampini¹, J H Müller¹,
D Wilkowski^{1,3}, E Arimondo^{1,4} and H Ritsch²

¹ INFN, Dipartimento di Fisica, Università di Pisa, Via Buonarroti 2, I-56127 Pisa, Italy

² Institut für Theoretische Physik, Universität Innsbruck, Technikerstraße 25,
6020 Innsbruck, Austria

E-mail: arimondo@df.unipi.it

Received 15 October 2002, in final form 9 January 2003

Published 2 April 2003

Online at stacks.iop.org/JOptB/5/S29

Abstract

We report the results of an experimental study on the interaction of cooled cesium atoms with the optical field of two standing waves having different wavelengths (852 and 894 nm) and opposite circular polarizations. The spatial modulation of the superposition of the two optical potentials and the polarization properties of this configuration are expected to produce cooling of the atoms and a spatial modulation of their density with the periodicity of the beat of the two wavelengths. We performed temperature measurements of the cesium sample and observed the density distribution of the atoms for several configurations of the standing wave by means of time-of-flight absorption imaging and fluorescence imaging techniques. Experimentally we could not observe a pronounced density modulation on the length scale of the superperiod. Reasons for this are revealed by a one-dimensional numerical simulation including the complexity of the full Zeeman structure of the cesium atoms. That simulation reproduces the experimental results for the temperatures and spatial confinement.

Keywords: Optical lattices, bichromatic cooling, spatial density modulation

(Some figures in this article are in colour only in the electronic version)

1. Introduction

Optical lattices represent an important quantum system for testing fundamental concepts of quantum physics, for producing spatial modulation of cold atom distributions and also for future applications in quantum computing [1]. In optical lattices created by a single standing-wave laser the optical potential produces an atomic spatial organization on the scale of half the optical wavelength, i.e. several hundred nanometres for most experiments, except those realized using the long wavelength light of a CO₂ laser [2]. In optical superlattices, created with several laser fields, the optical potential is modulated on a macroscopic scale, giving rise to a macroscopic atomic modulation [3–5].

³ Present address: Université de Nice, INLN, 1361 route de Lucioles,
F-06560 Valbonne, France.

⁴ Author to whom any correspondence should be addressed.

One-dimensional superlattices have been demonstrated with monochromatic standing waves by creating the macroscopic spatial potential modulation using small angles for the light beams [6, 7]. By creating an optical lattice with two colours, control over the superlattice structure is enhanced. In [8] periodic structures of sodium atoms were produced by a bichromatic laser combination, with frequencies near the D₁ and D₂ lines, using red-detuned lasers and the same polarization for both transitions. Dutta *et al* [9] demonstrated an enhancement to rubidium atom sub-Doppler laser cooling using a bichromatic standing wave, with cooling on the D₂ transition and repumping on the D₁ transition. Optical superlattices created by exposing laser cooled ⁸⁵Rb atoms to a bichromatic D₁, D₂ standing-wave light field were demonstrated by Görlitz *et al* [10]. Large red detuning was used for the D₂ laser and small blue detuning for the D₁ laser, with a linearly orthogonal linearly (lin ⊥ lin) polarization

scheme for the bichromatic components. These authors studied one- and three-dimensional superlattice configurations using an absorption imaging technique and observed an estimated contrast of 30% in the one-dimensional superlattice.

A different bichromatic standing-wave optical cooling scheme, the XV system (so-called because the pattern of the induced laser couplings resembled a superposition of the capital letters X and V), was presented by Alge *et al* [11, 12] based on the atomic interaction between a stronger σ^+ -polarized field and a weaker σ^- -polarized one. In that scheme the atoms are cooled through an efficient Sisyphus mechanism and trapped at those maxima of the stronger field where the second, weaker field has a node. It was predicted that, for the combinations of the $F_g = 1/2 \rightarrow F_e = 3/2$ and $F_g = 1/2 \rightarrow F_{e'} = 1/2$ optical transitions, the bichromatic scheme produces high local densities modulated at the beat frequency of the two involved modes.

In the present work we extend the XV cooling scheme to cesium atoms, applying a bichromatic standing wave based on the D_1 and D_2 excitations. The cesium bichromatic cooling scheme involves the $F_g = 4 \rightarrow F_e = 5, 4, 3$ optical transitions, with a Zeeman atomic structure more complicated than the one theoretically investigated previously. We have examined the application of the bichromatic XV scheme to cesium atoms for different sets of laser parameters. The experimental investigation made use of a microscope based telescope system with a resolution large enough to resolve the spatial modulation produced by the bichromatic scheme on the cesium atoms.

Section 2 recalls the basics of the XV scheme and its application to cesium atoms. Section 3 describes the experimental set-up with both the laser manipulation of the atoms and the imaging detection scheme. Section 4 reports the experimental results achieved in our investigation. Section 5 describes the results of numerical calculations for the steady state atomic distributions using a quantum rate equation approach for parameters close to those investigated in the experiment. Conclusions are presented in section 6.

2. XV scheme

Let us first briefly recall the idea of trapping and cooling neutral atoms in a one-dimensional optical superlattice [12]. This kind of an optical trap consists of two pairs of counter propagating σ^- and σ^+ polarized laser beams with slightly different wavevectors, coupled to different angular momentum transitions of the atom, as represented schematically in figure 1(a). The general idea of this laser configuration is to trap and cool the atoms in a periodical optical potential where the periodicity is given by the beat frequency of the two different laser frequencies, which produces a spatial modulation substantially larger than the wavelength. Given the wavelengths λ_1 and λ_2 of the applied laser, the superperiodicity Λ_{SP} created by this so-called bichromatic laser cooling scheme is given by

$$\Lambda_{SP} = \frac{1}{2} \frac{\lambda_1 \lambda_2}{\lambda_1 - \lambda_2}. \quad (1)$$

For a given number of atoms this spatial periodic confinement would lead to a substantially higher local phase space density.

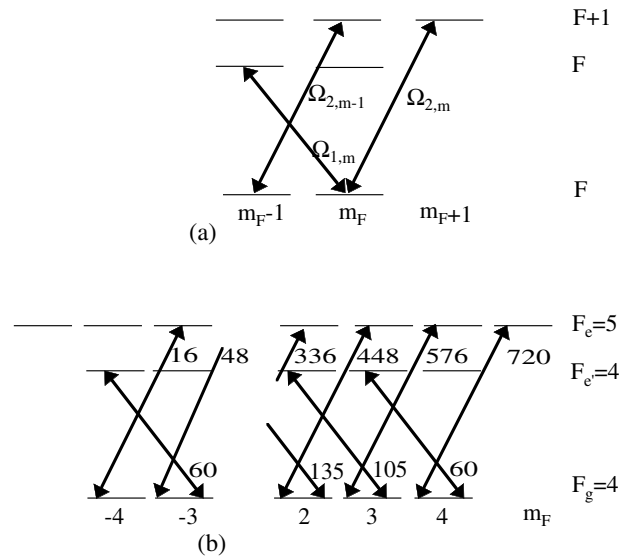


Figure 1. (a) Representation of the levels required for the XV scheme under σ^+ , σ^- excitations. The Rabi frequencies $\Omega_{i,m}$ including the corresponding Clebsch–Gordan coefficient, are indicated. (b) A few Zeeman levels of the $F_g = 4$ ground state ($m_F = -4, -3, 3, 4$), for the investigated cesium XV scheme with the σ^+ laser nearly resonant with $F_g = 4 \rightarrow F_e = 5$ transition and the σ^- laser nearly resonant with $F_g = 4 \rightarrow F_{e'} = 4$ transition. The transition strengths, normalized to 720, marked for the σ^+ and σ^- optical transitions, are proportional to the square of the Clebsch–Gordan coefficients determining the individual Rabi frequencies.

A central ingredient for the localization is the bichromatic force [3], which is a generalization of the optical dipole force for a bichromatic field. It can be rather strong, shows the desired periodicity and pushes the atoms towards or away from common antinodes of field depending on the relative atom field detunings on both transitions. However, as a second element, one needs an efficient cooling mechanism, to prevent the atoms being rapidly heated out again of the superpotential wells if the bichromatic force is active by itself. One possible way is to add spatially modulated cooling [9].

A concrete implementation of a bichromatic lattice with built-in cooling has been predicted for the case of a strong, far red detuned field combined with a near resonant blue-detuned field. Coupling of the red field to a $F_g \rightarrow F_e + 1$ transition generates the potential wells, while the blue field, acting on a $F_g \rightarrow F_e$ transition, provides for suitable optical pumping in these wells to facilitate atomic cooling. In this case the bichromatic force is not very strong, leading to only a weak modulation of the optical potential wells (see figure 2 derived from the analysis of section 5), but the cooling efficiency is also strongly spatially dependent [12]. Note that the $m = -4$ level experiences a much smaller light shift as it couples only to the σ^+ light with a much smaller Clebsch–Gordan coefficient. In combination, these two effects can still lead to atoms cooled well below the Doppler limit and very well localized on the superperiod scale Λ_{SP} . For an idealized XV level scheme, good localization and low temperatures were predicted for a large range of parameters [12], where the key parameters are the ratio of the maximum light shifts $|U_1/U_2|$ experienced by the atom in the two laser fields and the ratios of the maximum optical pumping rates γ_1/γ_2 induced by the two laser fields.

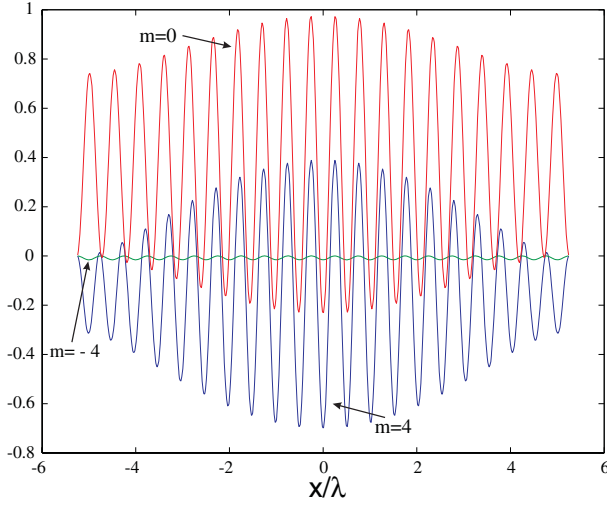


Figure 2. Adiabatic potentials, in units of $\hbar U_2$, for a few important Zeeman levels of the cesium $F_g = 4$ ground state in the XV scheme: $m_F = +4$ level in the lower line, $m_F = 0$ level in upper line and $m_F = -4$ level in middle line. The light shift is chosen negative on the D_2 -line and positive on D_1 with a ratio of $|U_1/U_2| = 2$. For better visibility the ratio of the laser wavevectors is set to $k_2/k_1 = 11/10$.

Good results are then expected if the red potential dominates but the pumping rates are still comparable.

We have investigated the XV bichromatic laser scheme of [12] adapted to the cesium atomic configuration, as shown in figure 1(b). The atoms were excited by two standing waves, composed by a σ^+ polarized laser acting on the $F_g = 4 \rightarrow F_e = 5$ hyperfine component of the D_2 transition, and a σ^- polarized laser acting on the $F_g = 4 \rightarrow F_{e'} = 4$ hyperfine component of the D_1 transition. In a few tests the σ^- polarized laser acted instead on the $F_g = 4 \rightarrow F_{e'} = 3$ hyperfine component of the D_1 transition. The position-dependent reduced Rabi frequency induced by the i th light field on the optical transition starting from the m ground state sublevel, including the corresponding Clebsch–Gordan coefficient will be denoted by $\Omega_{i,m} \cos k_i z$. We will define Ω_i as the Rabi frequency associated to the i laser field without including the appropriate Clebsch–Gordan coefficient. $\Delta_i = \omega_i - (E_{e_i} - E_g)$ will denote the detuning of that laser field from the atomic transition $g \rightarrow e_i$, with e_i referring to the D_i transition. The Zeeman structure of the lower and upper sublevels, represented in figure 1(b) makes the cesium level scheme more complex than the one investigated by Alge *et al* [12]. Thus for a preliminary analysis of the cesium XV cooling we decided, owing to the optical pumping process, to restrict our attention to the extreme ground Zeeman sublevels of the $F_g = 4$ state and the corresponding upper ones. This restricted level scheme was used to estimate the Rabi frequencies to be applied to the cesium atoms for the creation of the bichromatic cooling.

3. Experimental set-up

3.1. Laser manipulation

The set-up, essentially the five-beam magneto-optical trap (MOT) described in [14], was based on a glass cell containing low-pressure vapour of about 10^{-8} mbar produced by a

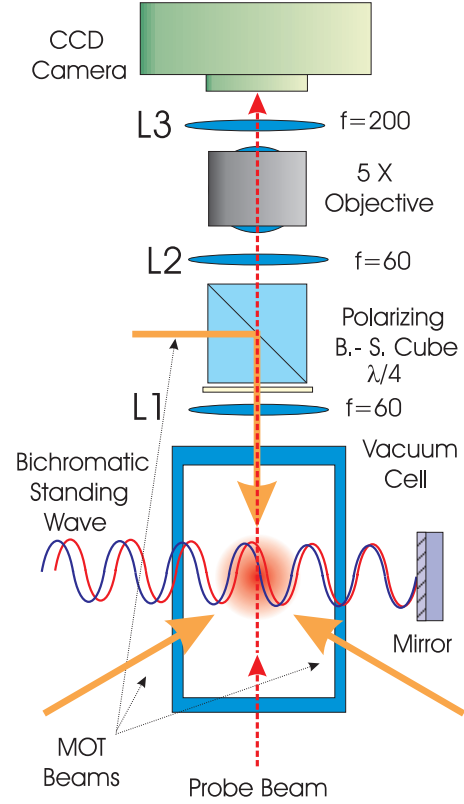


Figure 3. Experimental set-up with the three MOT laser beams propagating in the zy plane, one downwards the z axis and the remaining two at 120° . The bichromatic laser beams propagate along the y axis. Additional pairs of counterpropagating laser beams for cooling and repumping propagate along the x axis.

8 l s^{-1} ion pump. Cesium vapour was provided by thermal evaporation of some solid cesium stored in a side arm of the vacuum system. Since the cell and the laser sources were set out on mechanically decoupled optical tables, the laser radiation was brought in by means of polarization-conserving optical fibres. A pair of anti-Helmholtz coils externally attached to the vacuum cell produced the quadrupole magnetic field with a gradient of about 12.8 G cm^{-1} along the symmetry axis of the coils (the x axis in the horizontal axis of our reference system). The cell was located inside a μ -metal box, to suppress stray external magnetic fields disturbing the experiment.

The five-beam MOT was achieved by the intersection between two counterpropagating σ^+ and σ^- polarized laser beams disposed along the x axis and three σ^+ polarized beams lying on the y - z plane and intersecting with each other at an angle of 120° . One of these beams entered the cell downwards along the vertical direction (z axis), so the y axis of the system remained completely free from the MOT devices and could be used to operate the bichromatic standing wave, as schematically shown in figure 3. Each beam had a Gaussian profile with 4 mm waist and a maximum intensity of about 15 mW cm^{-2} . The trapping laser radiation was tuned to the red of the $F_g = 4 \rightarrow F_e = 5 D_2$ transition and was produced by diode lasers in master-slave configuration, with two cascaded slave lasers. The master diode laser, operating on an external cavity, was frequency stabilized through saturated absorption

spectroscopy. The first slave radiation could be shifted in frequency by means of a cat's-eye arrangement and in turn injected into the second slave laser. This provided the power required for the operation of the MOT, of the optical molasses and of the absorption imaging. A DBR laser (SDL-5702-H1) blue-detuned by about 5 MHz from the $F_g = 3 \rightarrow F_e = 3 D_2$ transition repumped the atoms lost by spontaneous decays into the $F_g = 3$ ground state. The repumping radiation, combined with the horizontal MOT beams on a polarizing beam-splitter cube, entered the cell along the x axis like the trapping circularly polarized beams, with about 3 mW of total power. During the MOT operation up to 1.5×10^7 Cs atoms were collected in a cloud with a diameter of about 1 mm in a time of about 1 s. After the MOT loading, the magnetic field was switched off in less than 100 μ s and the atoms were transferred into an optical molasses phase. During the molasses, the laser detuning was set to $-7\Gamma_{D_2}$, Γ_{D_2} being the linewidth of the D_2 transition, with the molasses beam intensity reduced to 30% of its value in the last 2 ms. After a molasses total duration time of 8 ms the atoms were cooled down to a temperature of about 5 μ K. We compensated the magnetic field acting on the atoms to better than 10 mG by examining the temperature and diffusion of the cloud under molasses conditions.

Finally the bichromatic standing wave was switched on for variable times between 100 μ s and 12 ms. The D_2 component of the bichromatic standing wave, tuned to the red of the $F_g = 4 \rightarrow F_e = 5$ transition with detuning Δ_2 , was produced by two diode lasers in master-slave configuration, providing up to 6.5 mW power, locked to a saturated absorption resonance. The D_1 component of the standing wave was produced by a SDL-57-S9726 DBR laser, locked to the $F_g = 4 \rightarrow F_{e'} = 4$ or $F_g = 4 \rightarrow F_{e'} = 3D_1$ transitions with a detuning Δ_1 varying between -2 and $4\Gamma_{D_1}$, a maximum power of about 4 mW reaching the vacuum cell. All the laser beams were controlled by acousto-optic modulators, allowing on/off switching times shorter than 1 μ s. The D_1 and D_2 laser beams, having initial orthogonal polarizations, were combined on a polarizing beam-splitter cube, then had their polarizations made σ^+ and σ^- respectively by a $\lambda/4$ plate and were sent into the cell and back-reflected along the y -direction. Both laser beams had a waist of 1.2 mm on the cesium atoms. In the alignment procedure much care was taken to have a precise spatial overlap of the two beams and to create the two standing waves in the horizontal plane to better than 0.1° .

The use of a common mirror for retroreflection mounted on a rigid support about 15 cm from the interaction region provided spatial stability of better than an optical wavelength over the timescales relevant for the experiment. Similarly, noise and drift of the two independently stabilized laser sources around their nominal frequencies could shift the standing-wave pattern at the synthetic wavelength Λ_{SP} by no more than 2% of its period assuming 10 MHz as a generous upper limit of the relative frequency excursion.

3.2. Imaging set-up

The cold atomic cloud was investigated using different imaging techniques: by time-of-flight absorption imaging, by *in situ* shadow imaging, by imaging the fluorescence light emitted

by the atoms residing within the bichromatic standing wave and, finally, by a dark-field diffraction technique. All images were acquired using a Princeton Instruments RTE/CCD-768-K CCD camera with a 768×512 grid of $9 \mu\text{m} \times 9 \mu\text{m}$ pixels.

For the time-of-flight absorption imaging, a probe laser beam resonant with the $F_g = 4 \rightarrow F_e = 5 D_2$ transition having variable duration between 20 and 80 μ s illuminated the cloud, whose shadow, projected onto the camera, gave information on the sample's spatial features. The probe beam, propagating vertically as shown in figure 3, was aligned orthogonally to the superlattice axis better than 0.5° . The time-of-flight imaging technique was also applied for the temperature measurements. The use of a lens system producing a 0.27 magnification factor allowed imaging of the whole sample after its ballistic expansion for time-of-flight durations up to 40 ms. The atomic temperatures, along the superlattice direction and along the orthogonal direction, were derived from measurements of the linear dimensions of the clouds after their expansion for variable times of flight.

For the *in situ* image of the atoms, since the spatial superperiod $\Lambda_{SP} = 9 \mu\text{m}$ produced by the 852 and 894 nm wavelengths was very close to the pixels' size, we enhanced the spatial resolution of the optical system, producing a magnification factor of five through a $5\times$ Mitutoyo microscope objective, as shown in figure 3 [15]. This detection scheme, allowing only a small area of the cloud to be investigated, was aligned to monitor the central part of the sample. The $5\times$ magnifying system imaged *in situ* the cold atom cloud on the CCD camera located above the MOT chamber. The two 6 cm focal length lenses L1 and L2 constitute a 1:1 telescope which relayed the cloud's image to the object plane of the microscope objective. The magnified image was then reconstructed on the CCD chip by the L3 lens. The image was focused on the CCD by varying the position of L1. The microscope objective set-up was also used to acquire fluorescence images of the atomic sample within the bichromatic lattice operation. To obtain fluorescence signals with acceptable signal to noise ratio, fluorescence images were accumulated on the CCD camera acquiring successive lattice images for a variable number (50–200) of experimental cycles.

We checked the spatial resolution of the detection set-up using a transmission grating with 10 μm spacing as a test pattern located at the position of the MOT. This test proved that the apparatus resolution detected spatial structures with dimensions of the order of the superlattice period. For the acquired images on the test pattern we measured an average contrast, C , of 0.5. The image contrast C was also measured by displacing the test grating a distance d , up to several millimetres from MOT centre, as shown in figure 4. The near independence of the C on d ensured that the focal depth of our set-up was large enough to detect a density modulation of the atomic sample at the superlattice period over the whole volume of the MOT.

A dark-field diffraction configuration, similar to that currently used by several research groups operating with Bose–Einstein condensates and, for instance, described in [16], was realized by replacing the objective with a 10 cm focal length lens having a black spot in the centre. In this configuration the unscattered part of the probe beam is blocked by the dark spot while diffracted light from the cloud is collimated. Any

Table 1. Measured temperatures for different parameters of the superlattice configuration and for different interaction times τ_{int} , with a σ^+ laser applied on the $D_2F_g = 4 \rightarrow F_{e''} = 5$ optical transition. A σ^- laser applied on the $D_1F_g = 4 \rightarrow F_{e''} = 4$ transition (datasets I–V) and on the $D_1F_g = 4 \rightarrow F_{e''} = 3$ transition (datasets IV–VI), was used.

| Data set | Ω_1/Γ_{D_1} | Δ_1/Γ_{D_1} | Ω_2/Γ_{D_2} | Δ_2/Γ_{D_2} | τ_{int} (ms) | T_{\parallel} (μK) | T_{\perp} (μK) | N/N_0 |
|----------|-------------------------|-------------------------|-------------------------|-------------------------|--------------------------|-----------------------------------|-------------------------------|------------|
| I | 2 | +3.3 | 5.9 | -39 | 4 | 580(60) | >500 | 0.65(0.13) |
| | | | | | 8 | 30(5) | 50(10) | 0.20(0.05) |
| II | 5.5 | +3.3 | 3.1 | -39 | 4 | 16(3) | 130(16) | 0.90(0.20) |
| | | | | | 8 | 80(15) | 105(15) | 0.75(0.15) |
| III | 2 | +2.2 | 1.7 | -16 | 8 | 31(10) | 50(10) | 0.90(0.20) |
| IV | 1.7 | +2.5 | 5.7 | -16 | 8 | 30(5) | 12(2) | 1.00(0.20) |
| V | 1.9 | -0.97 | 5.9 | -16 | 4 | >500 | 100(20) | 0.15(0.05) |
| VI | 1.9 | -2 | 5.9 | -16 | 4 | >500 | 60(15) | 0.15(0.05) |

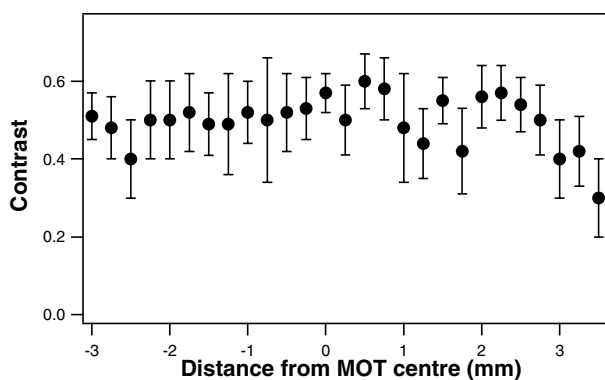


Figure 4. Contrast C measured on the test grating images as a function of the distance d from the focus position.

periodic small scale modulation of the optical density leads to distinct diffraction peaks at characteristic angles.

Using, again, the transmission grating as a test pattern we evaluated the performance of the system. Inserting various low quality optical windows along the beam path simulating the cell windows we checked that the resolution of the imaging system was not limited by the windows of the experimental apparatus.

4. Experimental results

The effects of the bichromatic standing wave on the cold cesium atoms were investigated for several sets of parameters varying the intensity and detuning of the two standing waves and for different interaction times. As a first step we verified the combined action of the two standing waves acting on the cold atoms after the molasses phase. Applying the D_2 standing wave alone nearly all of the atoms were lost from the interaction region even for an interaction time τ_{int} of about 1 ms. Instead when both D_2 and D_1 standing wave fields were present for properly chosen laser parameters the lattice was able to confine a substantial fraction of the atoms for interaction times τ_{int} up to⁵ 12 ms. We noticed that atom losses from the bichromatic lattice were mainly due to optical pumping into the $F_g = 3$ ground state. Generally the use of the maximum available power of the repumping laser minimized atom loss for all the standing-wave configurations we examined. In addition we

⁵ The acceleration due to dipole forces along the z -direction nearly compensates the gravitational acceleration so that the atoms are expected to fall slowly out of the interaction region.

observed a high sensitivity of the transverse shape and mean velocity of the cloud on alignment and intensity balance of the repumper beams along the x -direction. This behaviour is expected since about every second spontaneous emission event on the D_1 line optically pumps the atoms into the $F_g = 3$ ground states.

As a second step we searched for laser parameters of the bichromatic scheme where a steady state of the atomic distribution was reached during the interaction time. We required that during the 12 ms interaction time at least a substantial fraction of the atomic cloud remained confined along the direction of the superlattice and that little or no expansion was observed orthogonal to the lattice. Thus, under the required conditions, Sisyphus cooling along the laser direction is effective, while in the orthogonal direction heating due to spontaneous emission is not dramatic. We found confinement of the atoms along the lattice only when the D_1 laser was tuned to the blue side of the resonance, while for red detuning dramatic heating and fast diffusion of the cesium atoms along the lattice direction was observed.

In order to provide a characterization of the effect of the different laser parameters, we measured the velocity spread of the cloud by ballistic expansion after switching off the bichromatic field abruptly. We found that after the interaction with the bichromatic lattice the cesium cloud was always warmer than immediately after the optical molasses phase and usually the expansion rates along the lattice and orthogonal to it were rather different. We thus assigned separate temperature values to the cloud along the superlattice direction and orthogonal to it, T_{\parallel} and T_{\perp} respectively. Measured values of the temperatures are reported in table 1. Assigned temperatures of the order of 500 μK or higher represent lower limit estimates of the clouds real temperature, because for these samples the expansion rates were too fast to allow precise measurements. In addition, for the hot samples, we observed that the spatial distribution after time-of-flight was not well fitted by a single Gaussian curve, indicating a non-thermal velocity distribution [17]. In the last column of the table we report the fraction of atoms under the fitted curve with respect to the initial number of atoms after the optical molasses phase. For the parameters of dataset I we assigned a higher temperature after 4 ms of interaction time than after 8 ms. Looking at the fraction N/N_0 of remaining atoms this means that even if most of the atoms were strongly heated in the initial few microseconds of the lattice phase, at longer times a smaller but colder sample remained on a broad hot

background. For red detuning on the D_1 transition after short times the temperature was typically higher than $500 \mu\text{K}$ and no cold fraction remained after longer interaction times (see datasets V and VI of table 1). The most efficient confinement of the cold atom cloud was obtained for $\Delta_2 = -16\Gamma_{D_2}$ and $\Delta_1 = 2.5\Gamma_{D_1}$ and for Rabi frequencies $\Omega_2 = 5.7\Gamma_{D_2}$ and $\Omega_1 = 1.7\Gamma_{D_1}$ respectively (dataset IV of the table). For these parameters the fraction of atoms released from the optical molasses and confined by the standing wave was close to unity, while the cloud expansion rates remained almost stationary after $\tau_{\text{int}} = 4 \text{ ms}$. We checked also a different polarization configuration of two $\text{lin} \perp \text{lin}$ standing waves [10] and observed no confinement and fast diffusion in both directions for all tested laser parameters.

In addition to the temperature measurements we investigated the structure of the atomic density distribution on short spatial scales using the magnifying imaging setup. Both absorption imaging after variable interaction times with the superlattice ranging from 0.1 to 12 ms as well as fluorescence imaging during the cloud exposure to the standing wave were performed. For none of the parameter sets reported in table 1 did the density profile of the cloud show evidence of a modulation on the superlattice length scale. Fourier analysis of both absorption and fluorescence images revealed no components at the expected spatial frequencies above the detection noise. This observation combined with the previous test of the imaging system allowed us to exclude any modulation of the density distribution with a contrast greater than 10%. As a further test we analysed the light diffracted by the sample in a dark field configuration. Again we could not detect any distinct diffraction orders, confirming the overall homogeneity of the atomic cloud at the 10% level when coarse-grained over the optical wavelength.

5. Steady state distribution of optical superlattices

5.1. Model

Let us now theoretically analyse the bichromatic cooling and trapping for the case of the cesium atoms and try to interpret the experimental findings of this work. So far most theoretical work has concentrated on some hypothetical $1/2-3/2$ -level scheme (XV). Unfortunately one cannot directly apply these results here. In order to get some realistic theoretical estimates of the expected atom temperatures and localizations, we will have to use the full $F_g = 4 \rightarrow F_e = 5 \rightarrow F_{e'} = 4$ or the $F_g = 4 \rightarrow F_e = 5 \rightarrow F_{e'} = 3$ level manifold. This turns out to be necessary as the values of the Clebsch–Gordan coefficients in the system span a rather large range here. We can restrict ourselves to a quantum model of one-dimensional motion along the light field axis neglecting saturation effects. The main goal of our effort is to calculate the steady state distributions for the atomic positions and momenta using a quantum rate equation approach [13]. In addition this allows us to get good estimates of the spatial distribution of fluorescence.

The Hamiltonian of our model in the dipole and rotating wave approximation reads

$$H = \frac{\hat{p}^2}{2m} - \sum_{n=-F_k}^{F_k} \sum_{k=1,2} \hbar \Delta_k P_{e_{k,n}}$$

$$\begin{aligned} & - \frac{i}{2} \sum_{m=-F}^F \hbar \Omega_{1,m} (\alpha_1(\hat{x})^* |g, m\rangle \langle e_{1,m+1}| - \text{h.c.}) \\ & - \frac{i}{2} \sum_{m=-F}^F \hbar \Omega_{2,m} (\alpha_2(\hat{x})^* |g, m\rangle \langle e_{2,m-1}| - \text{h.c.}) \end{aligned} \quad (2)$$

Here k labels the chosen transitions, $P_{e_{k,n}}$ denotes the projector onto the atomic excited state $|e_{k,n}\rangle$ and $\Delta_k = \omega_{\text{laser}}^k - \omega_{ge_{k,n}}$ gives the detuning of the laser frequency relative to the corresponding atomic transition frequency. $\Omega_{k,m}$, as defined above, is the Rabi frequency induced by the k th laser on the respective sublevel transition including the corresponding Clebsch–Gordan coefficient. It has to be set to zero if the corresponding upper level does not exist. \hat{x} and \hat{p} stand for the position and momentum operators, respectively, in x -direction, which is defined by the direction of the incident laser beams. The functions

$$\alpha_1(x) = \sin(k_1 x), \quad (3)$$

$$\alpha_2(x) = \cos(k_2 x) \quad (4)$$

describe the spatial variation of the two circularly polarized laser fields with frequency ω_{laser}^n and wavevector k_n , where $n = 1, 2$. The first two terms of equation (2) give the kinetic energy and the internal atomic energy (in a rotating frame), whereas the third and the fourth term represent the interaction potentials between the atom and the σ_+ and σ_- polarized laser fields.

In the case of weak internal excitation of the atom, i.e. for saturation parameters $s_{k,m} = \frac{1}{2} \Omega_{k,m}^2 / (\Delta_k^2 + \Gamma_k^2/4)$ much less than unity (with Γ_n , the decay rates of the upper atomic levels), we can adiabatically eliminate all excited states and eventually end up with an effective master equation for the density matrix ρ :

$$\dot{\rho} = -i[H', \rho] + R\rho, \quad (5)$$

where H' describes the atoms moving in their effective dipole potentials and R describes the redistribution of atomic populations due to spontaneous emission. The details of this method are well known and established and can be found, for example, in [13, 18].

The adiabatic potentials which would be seen by a slow atom in a semiclassical picture are obtained by locally diagonalizing H' and depicting its eigenvalues. Due to the simple polarization geometry we use, this task is very easy. As an example we use the experimental dataset II of table 1 and in figure 2 plot the potentials corresponding to the $m_F = \pm 4$ and $m_F = 0$ Zeeman sublevels. Clearly all potentials show a superlattice with the desired periodicity Λ_{SP} . At $x = 0$ we have a common minimum for all the potentials, whereas the potential wells are shifted with respect to each other elsewhere. Hence a classical thermal distribution of the atoms would show localization around $x = 0$.

5.2. Stationary solution

In the following we will show the numerical results obtained for the stationary state of our system. Because of translational symmetry we restrict the calculation to a box in position space, $x \in [-L_b, L_b]$, whose length is an integer multiple of the superlattice period Λ_{SP} and assume periodic boundary

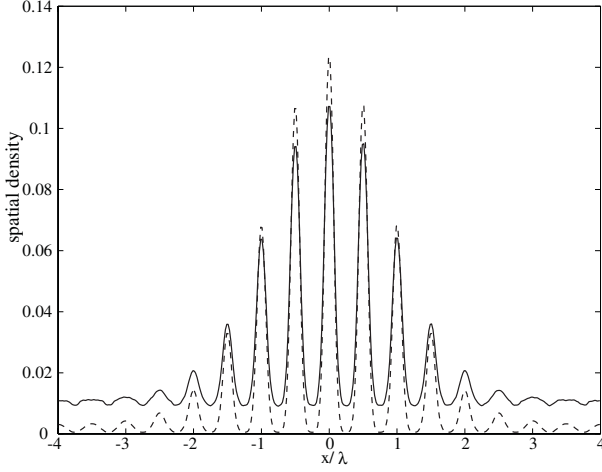


Figure 5. Distribution of atomic position density (solid curve) and total fluorescence (dashed curve) for $|U_1/U_2| = 2$, $k_1/k_2 = 15/16$ and $\gamma_1/\gamma_2 = 5$.

conditions. As a first step in the numerical treatment we calculate the eigenvectors $|n\rangle$ of H' on a discrete N -point spatial grid, i.e.:

$$H'|n\rangle = \epsilon_n|n\rangle \quad (6)$$

where n labels the $N_t = N(2F_g + 1)$ eigenstates. Next we write down the master equation (5) in the basis of these energy eigenstates $|n\rangle$

$$\dot{\rho}_{mn} = \sum_{k,l} \mathcal{L}_{(mn)(kl)} \rho_{kl} \quad (7)$$

where $\rho_{mn} = \langle m|\rho|n\rangle$ and the sum goes over all basis N_t vectors.

In a secular approximation we may now neglect all the coherences between states of different energies, which is valid if the energy levels are energetically separated, i.e. if the difference in energy exceeds the linewidth of the states. The resulting linear equations for the level populations can then be numerically inverted for the steady state. It is then fairly easy to extract the position and momentum distributions, the mean kinetic energies and the spatial distribution of atomic fluorescence. Although there are clear limitations, this method has proven very reliable in calculating position distributions and temperatures of atoms in standard optical lattice configurations [18, 19]. Let us first start with a sort of idealized parameter dataset, where we use 2:1 ratio of the optical potentials and 5:1 ratio of optical pumping rates for the maximally populated $m_F = \pm 4$ sublevel. As seen from figure 5 (solid curve) the atoms are well localized at the potential minima and also show a modulation on the superperiod scale. This is even better visible in the fluorescence distribution induced by the D_2 light (dashed curve) as the Clebsch–Gordan coefficient puts a strongly m_F -dependent weighting favouring the atoms in the $m_F = +4$ level, which possess an even better localization (see also figure 6).

In the following we will turn to the measured datasets. The atomic position distribution obtained this way for the dataset I of table 1 in the steady state is depicted in figure 6. We have plotted the contributions from atoms in different Zeeman sublevels separately to show that atoms are mainly pumped into

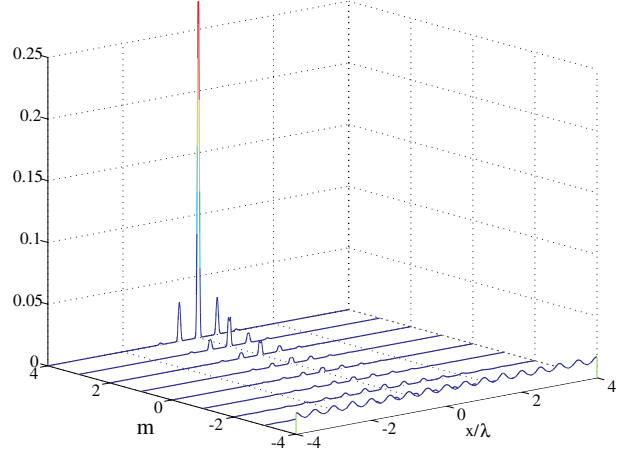


Figure 6. Stationary position distribution for experimental dataset I of table 1 split according to the different magnetic sublevels (m) of the $F_g = 4$ state. The parameters for the wavelengths were approximated by $k_1/k_2 = 15/16$.

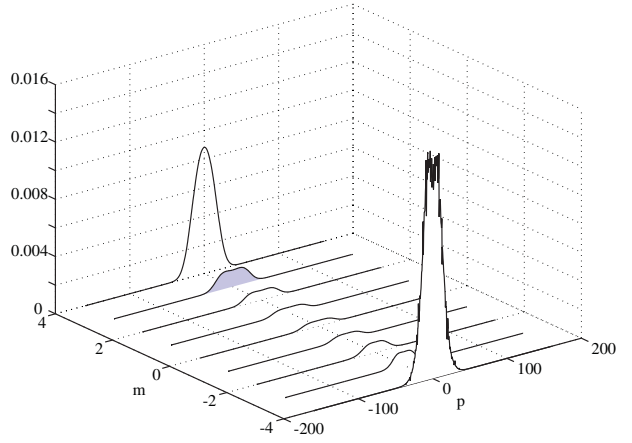


Figure 7. Stationary momentum distribution for experimental dataset I of table 1 for the various magnetic sublevels of the $F_g = 4$ state. The parameters for the wavelengths were approximated by $k_1/k_2 = 15/16$.

the two outermost sublevels, i.e. 30% in $m_F = 4$ and 47% in $m_F = -4$. While the atoms in the $m_F = +4$ are well localized, the $m_F = -4$ atoms are completely delocalized over the whole superperiod. As atoms in the $m_F = -4$ are decoupled from the σ^- light, the localization of the atoms in this case should be visible in the distribution of the atomic fluorescence as well. The momentum distributions for the atoms in these two states are shown in figure 7. This shows very similar widths corresponding to temperatures of $T_{+4} = 36 \mu\text{K}$ and $T_{-4} = 27 \mu\text{K}$, which gives a weighted average of $T = 32 \mu\text{K}$ in surprisingly good agreement with the longitudinal temperature measured for dataset I at long interaction times. If one looks at the radiative lifetimes (optical pumping times), the $m_F = -4$ state coupling only to the σ^+ field with a small Clebsch–Gordan coefficient, is more than two orders of magnitude smaller than for the $m_F = +4$ state. Hence steady state in these levels will be only reached very slowly, which could explain the high temperature observed for short measurement times, which is of the order of the energy the particles would get from the sudden initial turn on of the potential.

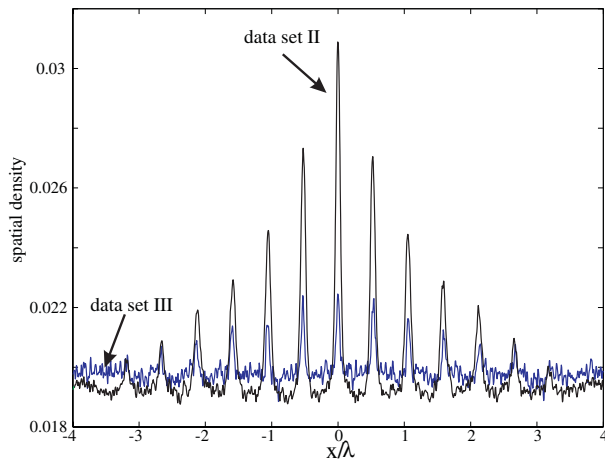


Figure 8. Stationary position distribution for the experimental datasets II and III of table 1. The parameters for the wavelengths were approximated by $k_1/k_2 = 15/16$.

The large magnitude difference of the Clebsch–Gordan coefficients is also responsible for the fact that the parameters for good cooling and good localization do not coincide very well for the $F_g = 4 \rightarrow F_e = 5$, and $\rightarrow F_{e'} = 4$ bichromatic field configuration. Where pumping rates provide a good spatial localization with respect to the superlattice on the $m_F = +4$ potential, a large part of the population is trapped at $m_F = -4$ as well, which is only marginally localized in position space. If on the other hand the parameters are chosen such that the population is pumped completely into $m_F = +4$, the laser cooling efficiency decreases. This reduces the lifetime of the atoms in the lattice and additionally diminishes superlattice localization. Where the transition from better localisation to better cooling occurs also strongly depends on the properties of the repumping mechanism, which could be used to get lower temperatures or better confinement.

The parameter regime where cooling dominates is realized for experimental datasets II and III of table 1. Here almost all the atoms are pumped into the $m_F = -4$ level and a limited superlattice localization of the atoms occurs but cooling is rather efficient. The total atomic position distribution for the two sets is shown in figure 8, giving a very limited contrast for dataset III, $C = 0.025$, and instead a reasonable one for dataset II, $C = 0.21$ (note the shift of the zero axis). Again due to the different Clebsch–Gordan coefficients, the fluorescence distribution differs from the position distribution, yielding somewhat more contrast than shown in figure 8 but still showing a strong background. To compare with the experimental results, however, the spatial distribution has to be averaged over the optical wavelength since the resolution of the imaging optics is limited to several micrometre. Doing this, the averaged contrast on the lengthscale of the superperiod drops to a mere $C_{av} = 0.03$ and thus below the detection noise, even for dataset II.

The bichromatic cooling is nevertheless active, yielding average kinetic temperatures of $T = 71 \mu\text{K}$ for the dataset II and $T = 24 \mu\text{K}$ for the dataset III, which again is in reasonable agreement with the measured values at long interaction times. As saturation effects are neglected some of the heating terms could be missing. Since in both latter cases most atoms are in the rather weakly coupled $m_F = -4$ level, the total

scattered light intensity is much lower than for the first set. Hence transverse heating is strongly reduced, yielding lower transverse temperatures.

6. Conclusions

The present experimental investigation of the XV cooling scheme on the cesium atoms with standing wave laser beams demonstrated that the associated bichromatic forces are efficient in producing low atomic temperatures along the laser propagation direction. That cooling was confirmed by the numerical simulations based on a one-dimensional model including the full complexity of the Zeeman sublevels of the cesium atoms but neglecting the saturation of the optical coherences. However, the cooling was realized for sets of laser parameters different from those predicted by the simplified level scheme introduced in a previous theoretical analysis [12]. The experimental investigation could not detect a spatial localization of the atoms in the bichromatic field on the lengthscale of the superperiod, giving an upper limit of 10% for the contrast in the density modulation. This result was confirmed by the numerical simulation. Our investigation shows that, owing to the Zeeman structure of the cesium atoms, cooling and localization cannot be reached simultaneously for the explored laser parameters.

Apart from a different polarization configuration, the important difference between the set-up in [10] and our set-up is the magnitude of the detuning used in the D_2 line. While we worked with a detuning smaller than or comparable with the excited state hyperfine splitting (hfs), in the Munich experiment a detuning much larger than the excited state hfs has been used. The huge detuning flattens out drastically the large difference in the effective Clebsch–Gordan coefficients between extreme Zeeman levels which, as discussed in the theoretical section, is responsible for the only poor localisation in the case of resolved hyperfine structure. Furthermore, at very large detunings, where the hfs can be ignored, one arrives to the original $J_g = 1/2 \rightarrow J_e = 3/2$ XV scheme. In future theoretical work we plan to include all excited state hyperfine levels into the model to systematically search for optimum parameters for simultaneous localisation and cooling and to test the above conjecture. One might consider also schemes with cooling and localisation phases separated in time in order to improve the localisation, and with additional confinement provided by laser dipole traps.

Acknowledgments

We thank A Di Stefano for setting up the experimental configurations in an early investigation. This work was supported by the INFN through the PRA Photonmatter Project and by the MIUR through the COFIN2000 Initiative. The collaboration between the two groups was financed by the European Commission through the Cold Quantum-Gases Network, contract HPRN-CT-2000-00125.

References

- [1] For reviews see
Jessen P S and Deutsch I H 1996 *Adv. At. Mol. Opt. Phys.* **37** 95
Meacher D R 1998 *Contemp. Phys.* **39** 329

- Grynberg G and Mennerat-Robilliard C 2001 *Phys. Rep.* **355** 335
- [2] Scheunemann R, Cataliotti F S, Hänsch T W and Weitz M 2000 *Phys. Rev. A* **62** R051801
- [3] Grimm R, Ovchinnikov Yu B, Sidorov A I and Letokhov V S 1990 *Phys. Rev. Lett.* **65** 1415
- [4] Grimm R, Söding J and Ovchinnikov Yu B 1995 *JETP Lett.* **61** 367
- [5] Pellizzari T and Ritsch H 1995 *Europhys. Lett.* **31** 133
- [6] Guidoni L and Verkerk P 1998 *Phys. Rev. A* **57** R1501
- [7] Schulze Th, Brezger B, Mertens R, Pivk M, Pfau T and Mlynek J 2000 *Appl. Phys. B* **70** 671
- [8] Milori D M B P, Martinez M A G, Tuboy A M, Marcassa L G, Flemming J, Ejnisman R, Zilio S C and Bagnato V S 1999 *Phys. Rev. A* **59** 3101
- [9] Dutta S K, Morrow N V and Raithel G 2000 *Phys. Rev. A* **62** 035401
- [10] Görlitz A, Kinoshita T, Hänsch T W and Hemmerich A 2001 *Phys. Rev. A* **64** 011401
- [11] Alge W, Ellinger K, Stecher H, Gheri K M and Ritsch H 1997 *Europhys. Lett.* **39** 491
- [12] Alge W, Gheri K M, Ellinger K, Stecher H and Ritsch H 1999 *Eur. Phys. J. D* **6** 133
- [13] Horak P and Ritsch H 1997 *J. Opt. Soc. Am. B* **14** 8
- [14] di Stefano A, Wilkowski D, Müller J H and Arimondo E 1999 *Appl. Phys. B* **69** 263
- [15] For a similar system see
Hau L V, Busch B D, Liu C, Dutton Z, Burns M M and Golovchenko J A 1998 *Phys. Rev. A* **58** R54
- [16] Bradley C C, Sackett C A and Hulet R G 1997 *Phys. Rev. Lett.* **78** 985
Anderson B P and Kasevich M A 1999 *Phys. Rev. A* **59** R938
- [17] Imaging the whole cloud at the same time gives us direct access to the spatial distribution, thus excluding systematic effects in conventional time-of-flight temperature measurements as discussed e.g. in
Brzozowski T M *et al* 2002 *J. Opt. B: Quantum Semiclass. Opt.* **4** 62
- [18] Castin Y and Dalibard J 1991 *Europhys. Lett.* **14** 761
- [19] Stecher H, Ritsch H, Zoller P, Sander F, Esslinger T and Hänsch T W 1997 *Phys. Rev. A* **55** 1997